Synthesis and Substitution Chemistry of Redox-Active Manganese/Cobalt Oxide Nanosheets

Nobuyuki Sakai,[*,†] Katsutoshi Fukuda,[‡] Renzhi Ma,[†] and Takayoshi Sasaki[*,†]

[†]International Center for Materials Nanoarchitectonics (WPI-MANA), National Institute for Materials Science (NIMS), 1-1 Namiki, Tsukuba, Ibaraki 305-0044, Japan and [‡]Office of Society-Academia Collaboration for Innovation, Kyoto University, Yoshida-honmachi, Sakyo-ku, Kyoto 606-8501, Japan.

ABSTRACT: We report the synthesis and electrochemical properties of Co-substituted manganese oxide nanosheets ($Mn_{1-x}Co_xO_2$). Polycrystalline samples of layered $Na_{0.6}Mn_{1-x}Co_xO_2$ (x = 0.2–0.5) were synthesized as starting materials. A linear decrease in the lattice constant a with increasing Co content supported the successful substitution of Co^{3+} ions for Mn^{3+} ions in the host layers. Acid-exchange treatment of the $Na_{0.6}Mn_{1-x}Co_xO_2$ powders resulted in the formation of H-$Mn_{1-x}Co_xO_2$ while preserving the Mn/Co ratio and layered structure. Exfoliation of H-$Mn_{1-x}Co_xO_2$ was achieved by reaction with tetra–*n*–butylammonium ions, yielding unilamellar $Mn_{1-x}Co_xO_2$ (x = 0.2–0.5) nanosheets with a thickness of 0.8 nm. The optical absorption peak of the obtained $Mn_{1-x}Co_xO_2$ nanosheets was continuously blueshifted as the Co content increased. The $Mn_{1-x}Co_xO_2$ nanosheets exhibited well-defined redox peaks, which were shifted to a negative potential with increasing Co content. These results suggest that the 3d orbitals of Mn and Co are mixed owing to their statistical distribution in the nanosheets. The $Mn_{1-x}Co_xO_2$ nanosheet electrodes showed a capacitance of 700–1000 F g^{-1} and improved cycle performance compared to MnO_2 nanosheets.

INTRODUCTION

Metal oxide nanosheets have received increasing attention because of their versatility for various applications owing to their properties based on their widely tunable composition and structure.[1–6] The oxide nanosheets can be obtained by exfoliating their mother layered crystals into each elementary layer. The resultant nanosheets have a thickness of ~1 nm, while the lateral size ranges from submicrometers to several tens of micrometers. Due to such unusually high two-dimensional (2D) morphologies, the nanosheets are expected to show unique electronic and physicochemical properties different from the corresponding bulk materials. For example, titania nanosheets exhibit a shift in the band edge that increases the band gap energy in comparison with their bulk counterparts due to quantum size effects.[7,8] Nanosheets with redox capabilities are promising for applications such as electrochemical capacitors and lithium-ion batteries because of their extremely large surface area. Such applications can be anticipated for nanosheets composed of RuO_2,[9,10] MnO_2,[11–16] CoO_2,[17–19] $Mn_{1/3}Co_{1/3}Ni_{1/3}O_2$,[20] etc. Ruthenic acid nanosheets have been reported to exhibit a capacitance as large as 658 F g^{-1}.[9] Reassembled nanosheets of MnO_2[21,22] or CoO_2[19] have been used as cathodes for lithium-ion batteries.

Modulation of the properties can be achieved by the elemental substitution or doping of the redox-active nanosheets, as has been reported for bulk materials. For example, the influence of cobalt doping on the electrochemical properties of layered manganese oxide has been studied to improve the cycle performance of lithium-ion batteries.[23–25] The doping of different elements into redox-active nanosheets and its effect on the crystal structure, optical properties, and redox properties have been scarcely examined, although such properties would be largely modified. Examples of redox-active nanosheets doped with different elements include MnO_2 nanosheets partly substituted with Co,[26] Co/Ni,[20] or Ru[27]. However, the redox properties have been examined only for Ru-substituted MnO_2 nanosheets. The doping of 10% ruthenium into MnO_2 nanosheets was reported to enhance the electrochemical capacitance of the reassembled material by ~40%.[27] Hence, doping is one method to improve the redox properties of nanosheets to make them favorable for applications such as energy-storage devices. Because ruthenium is a noble metal and expensive, the replacement of ruthenium with 3d transition metal elements as dopants is expected to lead to possibilities for the development of various energy-storage materials. Hence, it is of interest to examine the effect of cobalt substitution, as cobalt is a 3d transition metal, on the crystal and electronic structure of MnO_2 nanosheets.

In the present study, we synthesize Co-substituted MnO_2 nanosheets ($Mn_{1-x}Co_xO_2$) through the synthesis, protonation, and exfoliation of layered manganese oxide doped with cobalt. The starting material was synthesized by following the reported procedure.[23–25] Although protonation of the starting material has been studied, the influence of the doping amount on the crystal structure and the valence of constituent elements has not been report-

ed.[28] Although the synthesis of MnO_2 nanosheets doped with cobalt has been examined via a bottom-up process,[26] there is no direct evidence for the doping of Co into the lattice of MnO_2 nanosheets. In addition, the structural aspects and electrochemical properties have not been studied. In this work, we conduct a systematic investigation on the partial substitution of Co for Mn in layered Na-$Mn_{1-x}Co_xO_2$ and H-$Mn_{1-x}Co_xO_2$ structures, as well as $Mn_{1-x}Co_xO_2$ nanosheets, via various techniques, including X-ray diffraction (XRD), elemental analysis, X-ray absorption near edge structure (XANES), and X-ray photoelectron spectroscopy (XPS). The nanosheets obtained via exfoliation of the layered compound have a larger lateral size and higher crystallinity than those synthesized via the bottom-up process, which is beneficial for applications such as electrochemical devices. We also examine the lattice constants, optical properties, and electrochemical properties of the $Mn_{1-x}Co_xO_2$ nanosheets as a function of cobalt substitution, which may give insight into the crystal structure and electronic structure of the nanosheets.

EXPERIMENTAL SECTION

Reagents. All chemicals were of analytical grade and used as purchased. Milli-Q filtered water was used throughout the experiments.

Synthesis of $Na_{0.6}Mn_{1-x}Co_xO_2$. Layered compounds, $Na_{0.6}Mn_{1-x}Co_xO_2$ (x = 0.2, 0.3, 0.4, 0.5), as starting materials were synthesized via a solution route according to the literature.[23] $Mn(CH_3COO)_2{\cdot}4H_2O$, $Co(CH_3COO)_2{\cdot}4H_2O$, and $NaNO_3$ in a stoichiometric ratio (1–x:x:0.6) were dissolved in pure water and dried on a hot plate at 130 °C overnight. The resulting precipitates were pre-annealed in an oven at 300 °C for 20 h in air to decompose the organic components. Then, the materials were heated at 700 °C (x = 0.2), 730 °C (x = 0.3), 755 °C (x = 0.4), or 800 °C (x = 0.5) for 20 h in air and then quenched.

Protonation. The resulting black powder (2 g) of $Na_{0.6}Mn_{1-x}Co_xO_2$ was dispersed and shaken in 0.1 mol dm^{-3} HCl solution (400 cm^3) at room temperature. This procedure was repeated three times by renewing the acid solution every 24 h. The resulting acid-exchanged product was filtered, washed with pure water, and dried in air.

Exfoliation. A weighed amount (0.4 g) of the protonated form was dispersed in 100 cm^3 of aqueous tetra–*n*–butylammonium hydroxide (TBAOH) solution (12–20 mmol dm^{-3}). The resulting suspension was shaken moderately (120 rpm) for 2 weeks at ambient temperature and then centrifuged at 3000 rpm (1680 G) for 30 min to sediment/remove any unexfoliated material. The upper solution was collected to obtain a colloidal suspension of the nanosheets, which was dark green in color.

Film Fabrication. Si wafer substrates were cleaned by immersion in a bath of methanol/HCl (1:1 in volume) and then concentrated H_2SO_4 for 30 min each. Indium tin oxide (ITO)-coated quartz glass substrates with a flat surface (Kuramoto Co., Ltd., sheet resistance = 10 Ω/sq.) were cleaned by sonication in acetone, ethanol, and ultrapure water for 15 min each. Monolayer films were fabricated via a sequential adsorption procedure. First, the substrate was immersed in a polyethylenimine (PEI) solution (1.25 g dm^{-3}, pH 9) to make the surface positively charged. Then, the PEI-coated substrate was immersed in the colloidal suspension of nanosheets. The substrate was immersed in each solution for 20 min and then rinsed thoroughly with ultrapure water.

Characterization. The contents of Na, Mn, and Co in $Na_{0.6}Mn_{1-x}Co_xO_2$ and its acid-exchanged phases were determined by inductively coupled plasma (ICP) optical emission spectrometry (Hitachi, SPS3520UV-DD) after dissolving the sample in a mixed solution of HCl and H_2O_2. Thermogravimetric-differential thermal analysis (TG–DTA, Rigaku, TG-8120) was performed in the temperature range of 25–1000 °C at a heating rate of 10 °C min^{-1}. The mean valence of the oxidation state of Mn and Co in the samples was determined by redox titration.[15,29] The sample was dissolved in sulfuric acid containing an excess amount of sodium oxalate as a reducing agent. The residual sodium oxalate was titrated against the standard aqueous solution of potassium permanganate to deduce the mean valence of the oxidation state of the Mn and Co ions. XRD data were collected using a powder diffractometer (Rigaku, Ultima IV) with graphite monochromatized Cu Kα radiation (λ = 0.15405 nm). Scanning electron microscopy (SEM) observations were carried out using a microscope (JEOL, JSM-6010LA). Atomic force microscopy (AFM) images were collected in tapping mode using a Hitachi NanoNavi II Station and a SI-DF20 cantilever to examine the topography of the nanosheets deposited on the Si wafer substrate. Transmission electron microscopy (TEM) characterizations were performed on a JEOL JEM-3100F energy-filtering (Omega type) microscope. XPS measurements were performed on a PHI Quantera SXM (ULVAC-PHI) with an Al Kα source. In-plane XRD and XANES measurements were performed using synchrotron X-ray radiation at BL-6C, Photon Factory, High Energy Accelerator Research Organization. A spectrophotometer (Hitachi, U-4100) was employed to record the UV–vis absorption spectra. A potentiostat (Solartron, SI1287) was used for electrochemical measurements in a conventional three-electrode, single-compartment glass cell. An ITO substrate coated with $Mn_{1-x}Co_xO_2$ nanosheets served as the working electrode. The counter and reference electrodes were platinum wire and $Ag|Ag^+$, respectively. Propylene carbonate containing 0.1 mol dm^{-3} $LiClO_4$ was employed as the supporting electrolyte.

RESULTS AND DISCUSSION

Synthesis of $Na_{0.6}Mn_{1-x}Co_xO_2$. Figure 1a shows the XRD data of the obtained black powder of $Na_{0.6}Mn_{1-x}Co_xO_2$ (x = 0.2). All the diffraction peaks can be indexed to the rhombohedral structure [space group: $R\bar{3}m$ (No. 166)] with refined unit-cell parameters of a = 0.28642(1) nm and c = 1.6953(1) nm (Table S1). All samples including other compositions (x = 0.3–0.5) were obtained in a single phase based on the rhombohedral structure. The lattice constant a linearly decreased as the Co content (Co/(Mn+Co)) increased (Figure 2a), following Vegard's law. Hence, the crystal structure of the obtained

materials is the same as that of birnessite-type layered manganese oxide ($K_{0.45}MnO_2$) reported previously,[11,30] and Co substitutes at Mn sites in a statistical distribution on the MnO_2 planes of the crystals.

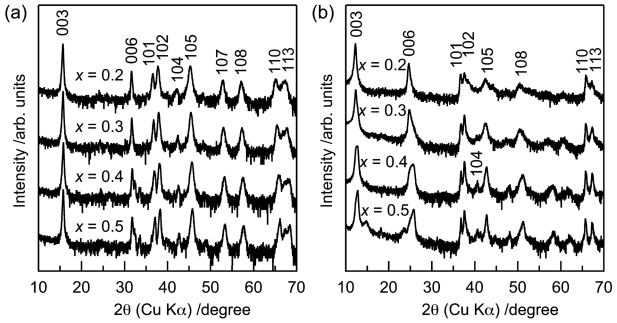

Figure 1. XRD patterns of (a) Co-doped layered manganese oxides, Na-$Mn_{1-x}Co_xO_2$ (x = 0.2, 0.3, 0.4, 0.5), and (b) their protonated materials, H-$Mn_{1-x}Co_xO_2$ (x = 0.2, 0.3, 0.4, 0.5). The XRD intensity is shown on a log scale.

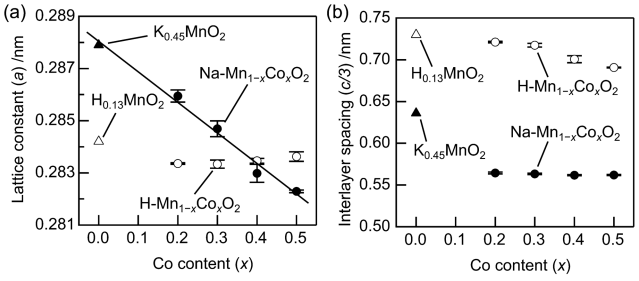

Figure 2. (a) Lattice constant a and (b) interlayer spacing $c/3$ of Na- (filled circle) and H- (open circle) $Mn_{1-x}Co_xO_2$ powders as a function of cobalt content (x). The data for x = 0.0 ($K_{0.45}MnO_2$ and $H_{0.13}MnO_2$) were taken from ref 11 and 32, respectively.

The chemical composition of the sample (x = 0.2) was determined to be $Na_{0.56}Mn_{0.81}Co_{0.19}O_2$ (Anal. Calcd: Na, 12.8%; Mn, 44.2%; Co, 11.1%. Found: Na, 13.0%; Mn, 44.7%; Co, 11.0%.) based on the results of elemental analysis by ICP and TG measurement. This formula agrees well with the nominal ratio of Na, Mn, and Co ions (0.6:0.8:0.2) during preparation. The composition of the other samples (x = 0.3–0.5) was also in good agreement with the preparation ratio of Na:Mn:Co = 0.6:1–x:x (Table 1). This formula also yields a negative charge of 0.56 per $Mn_{0.81}Co_{0.19}O_2$ layer. The redox titration with sodium oxalate suggested that the mean valence of Mn and Co, Z_{Mn+Co}, was 3.50, which is in good agreement with that estimated from the formula shown above (3.44). The slight difference in the mean valence (0.06, Figure S1) may be due to oxidation of the materials when dissolved in sulfuric acid during titration. Similar values of Z_{Mn+Co} were obtained among all compositions of Na-$Mn_{1-x}Co_xO_2$ synthesized (Table 1). This is compatible with the fact that the four samples have the same interlayer spacing of 0.57 nm (Figure 2b). Although the obtained Z_{Mn+Co} values are close to the Z_{Mn} value of $K_{0.45}MnO_2$, the interlayer spacing of $K_{0.45}MnO_2$ is larger by ~0.7 Å than that of Na-$Mn_{1-x}Co_xO_2$. This is reasonable because the ionic radius of K^+ (1.38 Å) in the interlayer space is larger by 0.36 Å than that of Na^+ (1.02 Å).[31]

Table 1. Composition of the Obtained Layered Crystals of Na-$Mn_{1-x}Co_xO_2$ and Their Protonated Materials and Mean Valence of Metal Ions Estimated by Chemical Titration

sample	as-synthesized		after protonation	
	composition	valence	composition	valence
x = 0.2	$Na_{0.56}Mn_{0.81}Co_{0.19}O_2$	3.50(3)	$H_{0.22}Na_{0.03}Mn_{0.82}Co_{0.18}O_2{\cdot}0.7H_2O$	3.75(3)
x = 0.3	$Na_{0.57}Mn_{0.72}Co_{0.28}O_2$	3.52(1)	$H_{0.30}Na_{0.04}Mn_{0.72}Co_{0.28}O_2{\cdot}0.8H_2O$	3.66(1)
x = 0.4	$Na_{0.56}Mn_{0.62}Co_{0.38}O_2$	3.53(1)	$H_{0.42}Na_{0.03}Mn_{0.62}Co_{0.38}O_2{\cdot}0.7H_2O$	3.55(1)
x = 0.5	$Na_{0.57}Mn_{0.52}Co_{0.48}O_2$	3.48(1)	$H_{0.48}Na_{0.02}Mn_{0.53}Co_{0.47}O_2{\cdot}0.7H_2O$	3.50(1)

To obtain quantitative information on the individual mean valence of Mn (Z_{Mn}) and Co (Z_{Co}), XANES spectra in Mn K-edge and Co K-edge regions were measured for the samples and the reference compounds (Figure 3). The profiles of the Co K-edge spectra of Na-$Mn_{1-x}Co_xO_2$ (x = 0.2–0.5) were similar to that of $LiCoO_2$ and overlapped with each other, suggesting that the Z_{Co} value is ~3 for all samples. In contrast, the profiles of Mn K-edge spectra were close to that of MnO_2 and slightly shifted to higher energy as the cobalt content increased. This result suggests that the Z_{Mn} value is close to 4 and increases with increasing cobalt content. Based on the composition ratios of Mn/Co and the Z_{Mn+Co} values deduced from the titration, assuming that Z_{Co} = 3, the Z_{Mn} values can be estimated to be 3.62, 3.72, 3.85, and 3.92 for x = 0.2, 0.3, 0.4, and 0.5, respectively (Table S2). The change in the Z_{Mn} value with composition is qualitatively consistent with the shift in the Mn K-edge spectra. The increase in the value of Z_{Mn} can be considered to be a result of the substitution of Co^{3+} for Mn^{3+}.

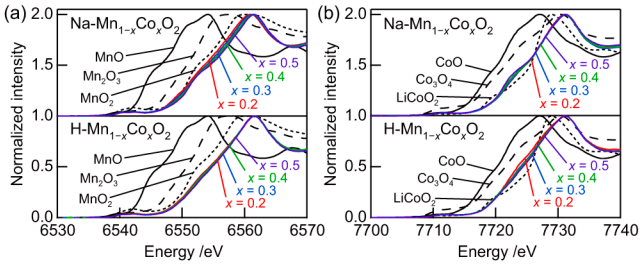

Figure 3. (a) Mn K-edge and (b) Co K-edge XANES spectra for Na-$Mn_{1-x}Co_xO_2$ and H-$Mn_{1-x}Co_xO_2$ (x = 0.2 (red lines), 0.3 (blue lines), 0.4 (green lines), and 0.5 (purple lines)) and the reference compounds.

The substitution of Co^{3+} for Mn^{3+} may induce the contraction of the average bond length of (Mn/Co)–O and hence the lattice constant a, because the ionic radius of low-spin Co^{3+} (0.545 Å) is smaller than that of high-spin Mn^{3+} (0.645 Å).[31] Although there are other combinations of high/low-spin Co^{3+}/Mn^{3+}, the estimated lattice constant a for low-spin Co^{3+} and high-spin Mn^{3+} is consistent with the experimental data (Figure S2). Based on the Mn/Co ratio, Z_{Mn}, and ionic radii of Co^{3+}, Mn^{3+}, Mn^{4+} (0.53 Å), and O^{2-} (1.36 Å), the average bond lengths can be estimated to

be 1.929, 1.917, 1.906, and 1.902 Å for x = 0.2, 0.3, 0.4, and 0.5, respectively (Table S2). The contraction ratios of the average bond lengths for x = 0.2, 0.3, 0.4, and 0.5 against that for $K_{0.45}MnO_2$ are 99.3%, 98.7%, 98.1%, and 97.9%, respectively, which are in good agreement with the contraction trend of lattice constant a (99.3%, 98.9%, 98.3%, and 98.0% for x = 0.2, 0.3, 0.4, and 0.5) (Table S2). Therefore, we conclude that the Mn^{3+} ions are substituted by Co^{3+} ions in the MnO_2 planes and the crystal structure of birnessite-type layered manganese oxide is preserved.

Protonation of $Na_{0.6}Mn_{1-x}Co_xO_2$. The protonation of Na-$Mn_{1-x}Co_xO_2$ (x = 0.2) was carried out by an acid leaching method. Based on the results of elemental analysis by ICP, TG measurement, and redox titration of the resulting material, H-$Mn_{1-x}Co_xO_2$ (x = 0.2), the composition was formulated to be $H_{0.22}Na_{0.03}Mn_{0.82}Co_{0.18}O_2{\cdot}0.7H_2O$ (Anal. Calcd: Na, 0.7%; Mn, 44.6%; Co, 10.5%; H_2O, 12.5%. Found: Na, 0.6%; Mn, 45.0%; Co, 10.7%; H_2O, 12.6%.) The proton content was deduced by considering the total charge neutrality. The protonated material contains ~0.7 mol H_2O in the interlayer space. The compositions of the other materials (x = 0.3–0.5) were also formulated in the same way (Table 1). The acid treatment significantly reduced the content of Na in the material, while the ratio of Mn to Co in the host layers was preserved upon treatment. The mean valence of Mn and Co, Z_{Mn+Co}, revealed by the redox titration ranged from 3.75 to 3.50 for x = 0.2 to 0.5 (Table 1). Each value is larger than that before the acid treatment (Figure S1), suggesting that acid leaching induces not only proton exchange but also the oxidative deintercalation of Na^+ ions, involving the disproportionation of Mn^{3+} to Mn^{4+} and Mn^{2+}, as has been demonstrated for various types of manganese oxides.[30]

The obtained H-$Mn_{1-x}Co_xO_2$ (x = 0.2) powder showed an XRD pattern that can be indexed to the rhombohedral structure [space group: R $\overline{3}$ m (No. 166)] (Figure 1b). The refined unit-cell parameters (a = 0.2834(1) nm, c = 2.165(3) nm, Table S3) are in good agreement with birnessite-type layered manganese oxide ($H_{0.13}MnO_2{\cdot}0.7H_2O$),[11,15,32] suggesting that the structure of the Co-substituted MnO_2 planes of the crystal remained intact upon protonation. The other compositions of H-$Mn_{1-x}Co_xO_2$ (x = 0.3–0.5) also have the same structural features (Figure 1b). The unit-cell parameter a was nearly constant for H-$Mn_{1-x}Co_xO_2$ powders with different cobalt contents (x), which is different from the results of Na-$Mn_{1-x}Co_xO_2$ (Figure 2a). Because the lattice constant a is correlated with the average bond length of (Mn/Co)–O, the average bond length can be estimated based on the composition ratio of Mn/Co and the Z_{Mn+Co} deduced from the titration, assumimg that Z_{Co} = 3. The Z_{Mn} values were estimated to be 3.91, 3.92, 3.89, and 3.94 for x = 0.2, 0.3, 0.4, and 0.5, respectively, which are similar to those for $H_{0.13}MnO_2{\cdot}0.7H_2O$ (Table S4).[11,32] The result that the Z_{Mn} values are almost invariable against different cobalt contents is compatible with the XANES study showing overlapping Mn K-edge spectra (Figure 3a). The average bond lengths can be estimated to be 1.901, 1.901, 1.904, and 1.901 Å for x = 0.2, 0.3, 0.4, and 0.5, respectively, which are in good agreement with the result that the lattice constant a is almost constant for the H-$Mn_{1-x}Co_xO_2$ powders with different cobalt contents (x) (Table S4).

The interlayer distance was expanded by 0.15 nm from 0.57 nm to 0.72 nm for the sample with x = 0.2 after protonation, as indicated by the shift of the basal diffraction peak to a lower angle (Figure 1). This change can be explained by the introduction of water molecules into the interlayer space since the water content increased upon protonation. Such increase in the interlayer distance was observed for the samples with other compositions (x = 0.3–0.5), although the expanded interlayer distance was dependent on the composition (Figure 2b). Because the amount of water content was almost the same, the difference in the interlayer distance is attributable to the difference in the mean valence of the metal ions. As the mean valence decreases with increasing cobalt content (x), the charge density of the host layers and the number of guest cations becomes large, resulting in a smaller interlayer spacing.

The samples were composed of plate-like crystals with lateral dimensions of 0.5–1 μm and 0.1–0.5 μm for the sample with x = 0.2 before and after the protonation, respectively (Figure S3). The decrease in the lateral size of the crystals is probably due to the dissolution of Mn^{2+} species produced by the disproportionation[30] of Mn^{3+} during acid leaching. Because the molar ratio of Mn to Co did not change after the protonation process (Table 1), Co^{2+} species are also dissolved during the protonation process, and the dissolution rates of Mn^{2+} and Co^{2+} are similar. The dissolution of Co^{2+} ions was quantitatively confirmed by a color change of the acid solution used for protonation (Figure S4). The dissolution of Co^{2+} is caused by the disproportionation of Co^{3+}, which should accompany the formation of Co^{4+}.[33–35] However, Co^{4+} can take one electron from Mn^{3+}, resulting in the formation of Co^{3+} and Mn^{4+} in the crystal, which is not contradictory to the assumption that all cobalt species are Co^{3+} on the basis of the XANES results. Moreover, the valence estimated from the dissolved amount of Co^{2+} and the process described above, Z_{Mn}', was consistent with that estimated from the titration and XANES studies (Table S5).

It is worth mentioning the different mechanisms of charge compensation against cobalt doping in Na-$Mn_{1-x}Co_xO_2$ and H-$Mn_{1-x}Co_xO_2$. In the former case, since the number of guest cations and the charge of the host layers are fixed against a change in the cobalt content, the change of the mean valence of Mn is required to maintain the charge neutrality of the crystal. In the latter case, because the number of guest cations is variable, the charge neutrality of the crystal can be maintained even without changing the mean valence of Mn.

Exfoliation of protonated H-$Mn_{1-x}Co_xO_2$. After shaking of the protonated samples dispersed in TBAOH solution (TBA^+/H^+ = ~1) and subsequent centrifugation of the suspension, the top solution was collected. The top solution was a colloidal suspension with a dark-green color. The suspension showed two broad absorption features in the UV–vis absorption spectrum (Figure 4a). One of the

features is an absorption peak at 368 nm for x = 0.2, which is similar to the spectrum of the MnO_2 nanosheet suspension. The molar extinction coefficient at the peak wavelength was estimated to be as large as ~10^4 mol^{-1} dm^3 cm^{-1}, which is equivalent to that for the MnO_2 nanosheets.[11,15] Such a large value is expected only for direct, allowed transitions. Hence, the absorption observed for the $Mn_{1-x}Co_xO_2$ nanosheets is ascribable to an electronic transition from the occupied band composed mostly of the oxygen 2p orbital to the unoccupied band composed mostly of the metal 3d orbital. The peak wavelength blueshifted as the Co content (x) increased (Figure 4b). Because the substitution of Mn for Co shifts the Fermi level of the metal band to more negative potential due to the increase in the number of electrons in the metal 3d orbitals, the energy required for the excitation should increase, resulting in the blueshifting of the absorption peak. The other feature is the appearance of an absorption shoulder at 600–700 nm. This absorption should be attributable to Co^{3+} species in the nanosheets because the undoped MnO_2 nanosheets do not have such absorption. These results support the homogeneous distribution of the Co ions into the MnO_2 lattice.

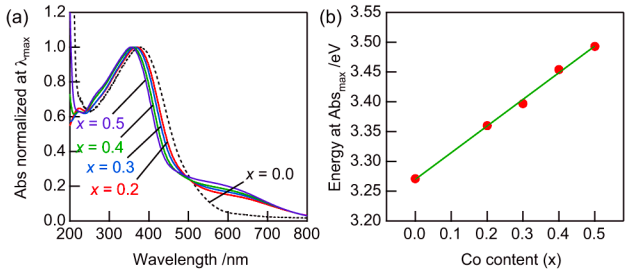

Figure 4. (a) UV–vis absorption spectra of colloidal suspensions of $Mn_{1-x}Co_xO_2$ (solid lines, x = 0.2, 0.3, 0.4, 0.5) and MnO_2 (dotted line) nanosheets. (b) Energy at the peak wavelength plotted as a function of Co content (x).

To examine the morphology, composition, and crystallinity, the exfoliated materials adsorbed on Si substrates pre-coated with polycations were investigated by AFM, XPS, and in-plane XRD. As shown in Figure 5a, AFM observation detected many 2D materials with uniform thickness of ~0.8 nm, which is comparable to that of undoped MnO_2 nanosheets.[11] The lateral size range from 100 to 500 nm is also compatible with that observed by TEM, as shown in Figure 5b. The ratios of Mn to Co in the $Mn_{1-x}Co_xO_2$ nanosheets revealed by XPS studies (Figure S5, Table S6) agreed well with those of the H-$Mn_{1-x}Co_xO_2$ powders, suggesting that the exfoliation process does not involve the change of the chemical composition of the host layers of H-$Mn_{1-x}Co_xO_2$. On the other hand, the in-plane XRD measurements (Figure 6) showed diffraction peaks, which are derived from the 2D hexagonal structure. The refined lattice constant a of the $Mn_{1-x}Co_xO_2$ (x = 0.2) nanosheets was 0.28384(4) nm, which is close to that before exfoliation (a = 0.2834(1) nm). Similar to the H-$Mn_{1-x}Co_xO_2$ powders, the lattice constant a was almost constant for the $Mn_{1-x}Co_xO_2$ nanosheets with different ratios (x) of Co/(Mn+Co), indicating that the 2D architecture remained substantially unchanged upon exfoliation. The smaller lattice constant a of the $Mn_{1-x}Co_xO_2$ nanosheets compared with that (a = 0.28593(5) nm) of MnO_2 nanosheets[32] is ascribable to the substitution of smaller Co^{3+} ions (0.545 Å) for larger Mn^{3+} ions (0.645 Å) in the MnO_2 nanosheets. Based on the results shown above, we conclude that $Mn_{1-x}Co_xO_2$ (x = 0.2–0.5) nanosheets with a plane composed of stoichiometric ratios of Mn and Co atoms sandwiched by two planes of hexagonally packed O atoms were obtained.

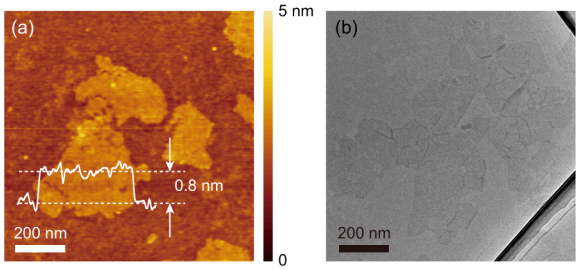

Figure 5. (a) Typical AFM image and height profile of exfoliated $Mn_{1-x}Co_xO_2$ (x = 0.2) nanosheets deposited on a Si substrate. (b) TEM image of exfoliated $Mn_{1-x}Co_xO_2$ (x = 0.2) nanosheets.

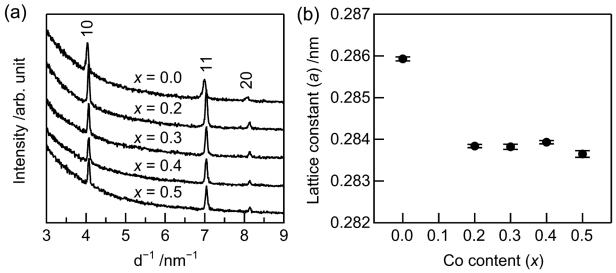

Figure 6. (a) In-plane XRD patterns of monolayer films of $Mn_{1-x}Co_xO_2$ (x = 0.2, 0.3, 0.4, 0.5) and MnO_2 nanosheets. The synchrotron X-ray wavelength was 0.12001 nm. (b) Refined lattice constants (a) of the $Mn_{1-x}Co_xO_2$ nanosheets plotted as a function of cobalt content (x).

Electrochemical properties of $Mn_{1-x}Co_xO_2$ nanosheets. Electrochemical studies of the $Mn_{1-x}Co_xO_2$ (x = 0.2–0.5) nanosheets were performed on monolayer films of the nanosheets fabricated on ITO substrates. Formation of the monolayer films was confirmed by AFM observation (Figure S6). Cyclic voltammograms (CV) in propylene carbonate containing 0.1 mol dm^{-3} $LiClO_4$ gradually changed with increasing number of potential sweeps, and CV curves under steady-state conditions were obtained after 100 cycles (Figure 7a, Figure S7). The relative capacitance of the $Mn_{1-x}Co_xO_2$ nanosheets gradually decreased with the number of potential sweeps and reached ~85% after 200 cycles, which is greater than that of the MnO_2 nanosheets, indicating that the cycle performance is improved by Co doping (Figure 7b). The in-plane XRD peaks were observed even after 200 cycles of potential sweeps (Figure S8), indicating that the 2D nanosheet structure was preserved. The CV curves of the $Mn_{1-x}Co_xO_2$ (x = 0.2–0.5) nanosheet electrodes showed well-defined reduction and oxidation peaks (Figure 7c), which are similar to those reported previously for MnO_2

nanosheet electrodes.[36] These peaks can be ascribed to the reduction/oxidation of the $Mn_{1-x}Co_xO_2$ nanosheets accompanied by the insertion/extraction of Li^+ ions. The fact that only one pair of redox peaks is observed implies the formation of mixed orbitals of Mn and Co. The redox potential for the $Mn_{1-x}Co_xO_2$ (x = 0.2) nanosheets was –0.42 V, which is more negative than that (–0.35 V) for MnO_2 nanosheets, and the redox potential linearly shifted in the negative direction as the cobalt content in the $Mn_{1-x}Co_xO_2$ nanosheets increased (Figure 7d). This result clearly indicates that the Fermi level of the $Mn_{1-x}Co_xO_2$ nanosheets shifts toward a more negative potential with increasing x, which is qualitatively consistent with the energy shift of the absorption peak upon changing the cobalt content, as shown in Figure 4. These results suggest that the 3d orbitals of Mn and Co are mixed owing to their statistical distribution in the nanosheets. The magnitude of the redox potential shift, however, was almost half of that of the absorption peak energy. The redox potential shift is reflected only by the Fermi level shift, while the absorption energy shift is based on the shifts of both the excited state and the ground state. These results suggest that the substitution of Co^{3+} for Mn^{3+} shifts the energy level of the highest edge of the occupied band, which is the origin of the electronic excitation, toward a more positive potential. In addition to the faradaic peaks, the $Mn_{1-x}Co_xO_2$ nanosheet electrodes showed capacitive currents, similar to the MnO_2 nanosheet electrodes. The capacitance was estimated to be 700–1000 F g^{-1} on the assumption that the electrode is covered with a perfect monolayer film of nanosheets. This value is greater than that reported for $Mn_{1-x}Ru_xO_2$ nanosheets (360 F g^{-1}),[27] although the electrode system is different. The previous study examined restacked composites of the nanosheets, whereas the present study examined monolayer films of nanosheets. It is also important to investigate the electrochemical capacitive properties of a single nanosheet. The present study clarified that $Mn_{1-x}Co_xO_2$ nanosheets are promising candidates for electrochemical capacitors with high energy density and high cycle performance.

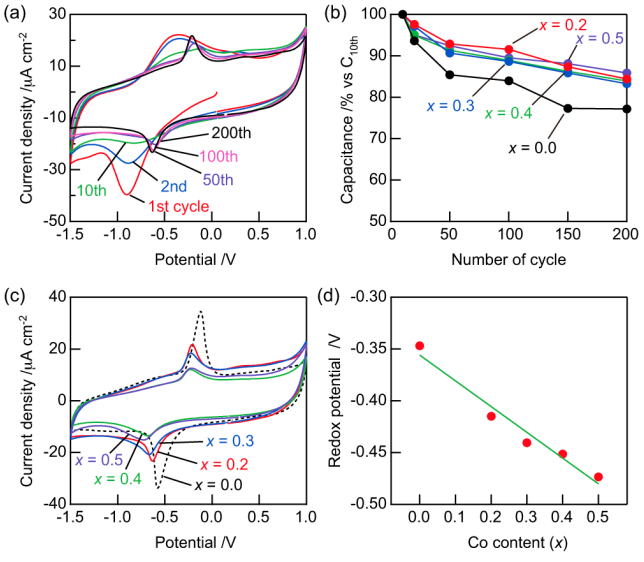

Figure 7. (a) Cyclic voltammograms of monolayer films of $Mn_{1-x}Co_xO_2$ (x = 0.2) nanosheet electrodes in a propylene carbonate solution containing 0.1 mol dm^{-3} $LiClO_4$ at a sweep rate of 50 mV s^{-1}. (b) Capacitance changes with potential sweeps. (c) Cyclic voltammograms of monolayer films of $Mn_{1-x}Co_xO_2$ (x = 0.2, 0.3, 0.4, 0.5) and MnO_2 (dotted line) nanosheet electrodes after 200 cycles. (d) Redox potential of $Mn_{1-x}Co_xO_2$ (x = 0.2, 0.3, 0.4, 0.5) and MnO_2 nanosheets plotted as a function of cobalt content (x). The potential values are given with respect to $Ag|Ag^+$.

CONCLUSIONS

In the present work, we successfully synthesized Co-substituted MnO_2 nanosheets with a composition of $Mn_{1-x}Co_xO_2$ (x = 0.2–0.5) by exfoliating the protonated form of $Na_{0.6}Mn_{1-x}Co_xO_2$ and studied the electrochemical properties of the exfoliated $Mn_{1-x}Co_xO_2$ nanosheets. Protonation can be achieved along with the preservation of the chemical composition of the host layers of the starting material. We clarified different charge compensation mechanisms against cobalt doping in the two different systems, Na-$Mn_{1-x}Co_xO_2$ and H-$Mn_{1-x}Co_xO_2$. The ratio of Mn to Co did not change upon exfoliation, yielding $Mn_{1-x}Co_xO_2$ (x = 0.2–0.5) nanosheets with a plane composed of stoichiometric ratios of Mn and Co atoms sandwiched by two planes of hexagonally aligned O atoms. The obtained $Mn_{1-x}Co_xO_2$ nanosheets showed improved cycle performance compared to MnO_2 nanosheets and higher capacitance than the $Mn_{1-x}Ru_xO_2$ nanosheets, making them favorable for applications such as energy-storage devices.

ASSOCIATED CONTENT

Supporting Information

The Supporting Information is available free of charge on the ACS Publications website.

Refinement data for XRD patterns of Na-$Mn_{1-x}Co_xO_2$ and H-$Mn_{1-x}Co_xO_2$. Estimated interatomic distance of (Mn/Co)–O based on valence and ionic radii for Na-$Mn_{1-x}Co_xO_2$ and H-$Mn_{1-x}Co_xO_2$. Valence of Mn for H-$Mn_{1-x}Co_xO_2$ estimated from the amount of dissolved Co^{2+} ions. Mean valence of metal ions deduced by chemical titration or Na content. Lattice constants estimated on the basis of bond length. SEM images of the samples. XPS of $Mn_{1-x}Co_xO_2$ nanosheets on Si. AFM images of a monolayer film of $Mn_{1-x}Co_xO_2$ nanosheets on ITO. Changes of CV curves. In-plane XRD of $Mn_{1-x}Co_xO_2$ nanosheets after CV. (PDF)

AUTHOR INFORMATION

Corresponding Author

*E-mail: (N.S.) sakai.nobuyuki@nims.go.jp
*E-mail: (T.S.) sasaki.takayoshi@nims.go.jp

ACKNOWLEDGMENT

This work was partly supported by the World Premier International Research Center Initiative on Materials Nanoarchitectonics (WPI-MANA), MEXT, Japan. N.S. acknowledges support from JSPS KAKENHI Grant Number JP16K14428. A part of this work was performed under the approval of the Photon Factory Program Advisory Committee (Proposal No.

2014G571). We would like to thank Prof. Izumi Nakai and Ms. Chizuru Ohishi (Tokyo Univ. of Science) for their preliminary work relating to this study. We also acknowledge Mr. Satoshi Takenouchi and Mr. Hirohito Ohata (NIMS) for ICP and XPS analyses, respectively.

REFERENCES

(1) Schaak, R. E.; Mallouk, T. E. Perovskites by Design: A Toolbox of Solid-State Reactions. *Chem. Mater.* **2002**, *14*, 1455–1471.

(2) Sasaki, T. Fabrication of Nanostructured Functional Materials Using Exfoliated Nanosheets as a Building Block. *J. Ceram. Soc. Jpn.* **2007**, *115*, 9–16.

(3) Osada, M.; Sasaki, T. Exfoliated Oxide Nanosheets: New Solution to Nanoelectronics. *J. Mater. Chem.* **2009**, *19*, 2503–2511.

(4) Ma, R.; Sasaki, T. Nanosheets of Oxides and Hydroxides: Ultimate 2D Charge-Bearing Functional Crystallites. *Adv. Mater.* **2010**, *22*, 5082–5104.

(5) Wang, L. Z.; Sasaki, T. Titanium Oxide Nanosheets: Graphene Analogues with Versatile Functionalities. *Chem. Rev.* **2014**, *114*, 9455–9486.

(6) Ma, R.; Sasaki, T. Two-Dimensional Oxide and Hydroxide Nanosheets: Controllable High-Quality Exfoliation, Molecular Assembly, and Exploration of Functionality. *Acc. Chem. Res.* **2015**, *48*, 136–143.

(7) Sasaki, T.; Watanabe, M. Semiconductor Nanosheet Crystallites of Quasi-TiO_2 and Their Optical Properties. *J. Phys. Chem. B* **1997**, *101*, 10159–10161.

(8) Sakai, N.; Ebina, Y.; Takada, K.; Sasaki, T. Electronic Band Structure of Titania Semiconductor Nanosheets Revealed by Electrochemical and Photoelectrochemical Studies. *J. Am. Chem. Soc.* **2004**, *126*, 5851–5858.

(9) Sugimoto, W.; Iwata, H.; Yasunaga, Y.; Murakami, Y.; Takasu, Y. Preparation of Ruthenic Acid Nanosheets and Utilization of Its Interlayer Surface for Electrochemical Energy Storage. *Angew. Chem., Int. Ed.* **2003**, *42*, 4092–4096.

(10) Fukuda, K.; Saida, T.; Sato, J.; Yonezawa, M.; Takasu, Y.; Sugimoto, W. Synthesis of Nanosheet Crystallites of Ruthenate with an α-$NaFeO_2$-Related Structure and Its Electrochemical Supercapacitor Property. *Inorg. Chem.* **2010**, *49*, 4391–4393.

(11) Omomo, Y.; Sasaki, T.; Wang, L. Z.; Watanabe, M. Redoxable Nanosheet Crystallites of MnO_2 Derived via Delamination of a Layered Manganese Oxide. *J. Am. Chem. Soc.* **2003**, *125*, 3568–3575.

(12) Liu, Z.-H.; Ooi, K.; Kanoh, H.; Tang, W.-P.; Tomida, T. Swelling and Delamination Behaviors of Birnessite-Type Manganese Oxide by Intercalation of Tetraalkylammonium Ions. *Langmuir* **2000**, *16*, 4154–4164.

(13) Wang, L. Z.; Omomo, Y.; Sakai, N.; Fukuda, K.; Nakai, I.; Ebina, Y.; Takada, K.; Watanabe, M.; Sasaki, T. Fabrication and Characterization of Multilayer Ultrathin Films of Exfoliated MnO_2 Nanosheets and Polycations. *Chem. Mater.* **2003**, *15*, 2873–2878.

(14) Yang, X.; Makita, Y.; Liu, Z.-H.; Sakane, K.; Ooi, K. Structural Characterization of Self-Assembled MnO_2 Nanosheets from Birnessite Manganese Oxide Single Crystals. *Chem. Mater.* **2004**, *16*, 5581–5588.

(15) Liu, Z.; Ma, R.; Ebina, Y.; Takada, K.; Sasaki, T. Synthesis and Delamination of Layered Manganese Oxide Nanobelts. *Chem. Mater.* **2007**, *19*, 6504–6512.

(16) Kai, K.; Yoshida, Y.; Kageyama, H.; Saito, G.; Ishigaki, T.; Furukawa, Y.; Kawamata, J. Room-Temperature Synthesis of Manganese Oxide Monosheets. *J. Am. Chem. Soc.* **2008**, *130*, 15938–15943.

(17) Masuda, Y.; Hamada, Y.; Seo, W. S.; Koumoto, K. Exfoliation of Layers in Na_xCoO_2. *J. Nanosci. Nanotechnol.* **2006**, *6*, 1632–1638.

(18) Kim, T. W.; Oh, E.-J.; Jee, A.-Y.; Lim, S. T.; Park, D. H.; Lee, M.; Hyun, S.-H.; Choy, J.-H.; Hwang, S.-J. Soft-Chemical Exfoliation Route to Layered Cobalt Oxide Monolayers and Its Application for Film Deposition and Nanoparticle Synthesis. *Chem. Eur. J.* **2009**, *15*, 10752–10761.

(19) Cheng, Q.; Yang, T.; Li, Y.; Li, M.; Chan, C. K. Oxidation-Reduction Assisted Exfoliation of $LiCoO_2$ into Nanosheets and Reassembly into Functional Li-Ion Battery Cathodes. *J. Mater. Chem. A* **2016**, *4*, 6902–6910.

(20) Oh, E.-J.; Kim, T. W.; Lee, K. M.; Song, M.-S.; Jee, A.-Y.; Lim, S. T.; Ha, H.-W.; Lee, M.; Choy, J.-H.; Hwang, S.-J. Unilamellar Nanosheet of Layered Manganese Cobalt Nickel Oxide and Its Heterolayered Film with Polycations. *ACS Nano* **2010**, *4*, 4437–4444.

(21) Wang, L. Z.; Takada, K.; Kajiyama, A.; Onoda, M.; Michiue, Y.; Zhang, L.-Q.; Watanabe, M.; Sasaki, T. Synthesis of a Li-Mn-Oxide with Disordered Layer Stacking through Flocculation of Exfoliated MnO_2 Nanosheets, and Its Electrochemical Properties. *Chem. Mater.* **2003**, *15*, 4508–4514.

(22) Suzuki, S.; Takahashi, S.; Sato, K.; Miyayama, M. High-Rate Electrode Properties of Li-Mn-Oxide Synthesized by Reassembly of MnO_2 Nanosheets for Li-Ion Battery. *Key Eng. Mater.* **2006**, *320*, 223–226.

(23) Armstrong, A. R.; Robertson, A. D.; Gitzendanner, R.; Bruce, P. G. The Layered Intercalation Compounds $Li(Mn_{1-y}Co_y)O_2$: Positive Electrode Materials for Lithium-Ion Batteries. *J. Solid State Chem.* **1999**, *145*, 549–556.

(24) Franger, S.; Bach, S.; Pereira-Ramos, J.P.; Baffier, N. Influence of Cobalt Ions on the Electrochemical Properties of Lamellar Manganese Oxides. *Ionics* **2000**, *6*, 470–476.

(25) Tsuda, M.; Arai, H.; Sakurai, Y. Improved Cyclability of Na-Birnessite Partially Substituted by Cobalt. *J. Power Sources* **2002**, *110*, 52–56.

(26) Kai, K.; Cuisinier, M.; Yoshida, Y.; Saito, G.; Kobayashi, Y.; Kageyama, H. One-Pot Synthesis of Co-Substituted Manganese Oxide Nanosheets and Physical Properties of Lamellar Aggregates. *Mater. Res. Bull.* **2012**, *47*, 3855–3859.

(27) Kim, S.-J.; Kim, I. Y.; Patil, S. B.; Oh, S. M.; Lee, N.-S.; Hwang, S.-J. Composition-Tailored 2D $Mn_{1-x}Ru_xO_2$ Nanosheets and Their Reassembled Nanocomposites: Improvement of Electrode Performance upon Ru Substitution. *Chem. Eur. J.* **2014**, *20*, 5132–5140.

(28) Takei, T.; Dong, Q.; Yonesaki, Y.; Kumada, N.; Kinomura, N. Synthesis and Electronic Structure of Proton-Type Partially Substituted Birnessite by Period-Four Transition Metal. *Mater. Res. Bull.* **2011**, *46*, 1896–1901.

(29) Takada, K.; Sakurai, H.; Takayama-Muromachi, E.; Izumi, F.; Dilanian, R.A.; Sasaki, T. A New Superconducting Phase of Sodium Cobalt Oxide. *Adv. Mater.* **2004**, *16*, 1901–1905.

(30) Feng, Q.; Kanoh, H.; Ooi, K. Manganese Oxide Porous Crystals. *J. Mater. Chem.* **1999**, *9*, 319–333.

(31) Shannon, R. D. Revised Effective Ionic Radii and Systematic Studies of Interatomic Distances in Halides and Chalcogenides. *Acta Cryst. A* **1976**, *32*, 751–767.

(32) Fukuda, K.; Nakai, I.; Ebina, Y.; Tanaka, M.; Mori, T.; Sasaki, T. Structure Analysis of Exfoliated Unilamellar Crystallites of Manganese Oxide Nanosheets. *J. Phys. Chem. B* **2006**, *110*, 17070–17075.

(33) Wizansky, A. R.; Rauch, P. E.; Disalvo, F. J. Powerful Oxidizing Agents for the Oxidative Deintercalation of Lithium from Transition-Metal Oxides. *J. Solid State Chem.* **1989**, *81*, 203–207.

(34) Gupta, R.; Manthiram, A. Chemical Extraction of Lithium from Layered $LiCoO_2$. *J. Solid State Chem.* **1996**, *121*, 483–491.

(35) Ren, Z.; Wang, Y.-W.; Liu, S.; Wang, J.; Xu, Z.-A.; Cao, G.-H. Synthesis of Cobalt Oxyhydrate Superconductor through a Disproportionation Reaction Route. *Chem. Mater.* **2005**, *17*, 1501–1504.

(36) Sakai, N.; Ebina, Y.; Takada, K.; Sasaki, T. Electrochromic Films Composed of MnO_2 Nanosheets with Controlled Optical Density and High Coloration Efficiency. *J. Electrochem. Soc.* **2005**, *152*, E384–E389.

Table of Contents.